Magnetic and transport properties, and the phase diagram of hole-doped $La_{1-x}Mg_xMnO_3$ ($x \leq 0.4$)

2001 J. Phys.: Condens. Matter 13 9349

(http://iopscience.iop.org/0953-8984/13/41/321)

INSTITUTE OF PHYSICS PUBLISHING JOURNAL OF PHYSICS: CONDENSED MATTER

J. Phys.: Condens. Matter **13** (2001) 9349–9367 PII: S0953-8984(01)25719-1

Magnetic and transport properties, and the phase diagram of hole-doped $La_{1-x}Mg_xMnO_3$ ($x \leqslant 0.4$)

J H Zhao, H P Kunkel, X Z Zhou and Gwyn Williams

Department of Physics and Astronomy, University of Manitoba, Winnipeg, Manitoba, Canada R3T 2N2

Received 12 June 2001
Published 28 September 2001
Online at stacks.iop.org/JPhysCM/13/9349

Abstract

A summary of detailed measurements of the field- and temperature-dependent ac susceptibility, the field-cooled and zero-field cooled magnetization, coercive field and the resistivity in zero field and applied field of 1.5 T is presented for hole-doped $La_{1-x}Mg_xMnO_3$ ($0.05 \leqslant x \leqslant 0.4$). Measurements of the ac susceptibility enable estimates of the (effective) critical exponents γ, β and δ to be made, which, when combined with the magnetization data, enable a phase diagram to be proposed. The transport data highlight the suppression of a metal–insulator transition in these systems with small average A-site radius. Furthermore, the transport behaviour is shown to be consistent with the predictions for charge transport by conventional small polaron hopping in both the paramagnetic *and* ferromagnetic phases, but inconsistent with recent quantitative predictions for magnetic small polaron-mediated conduction in a phase-separated picture.

1. Introduction

The behaviour of mixed valent manganese perovskites and manganese containing pyrochlores has been the subject of much recent study [1, 2]. Such interest has arisen not only due to their potential application as field sensors, fuel cells, etc, but also because of the fundamental questions that an explanation of their properties would answer. These systems exhibit colossal magnetoresistance (CMR) in addition to charge [3] and orbital ordering [4], possible spontaneous electronic phase separation [5] and magnetic frustration [6]. This behaviour is exemplified by rich electronic/magnetic phase diagrams which result, for example, from divalent cation (A) doping of the lanthanum manganites ($La_{1-x}A_xMnO_3$), typified by the $La_{1-x}Ca_xMnO_3$ system, one of the most extensively studied to date [7].

Here we report magnetic and transport measurements from which a phase diagram of the $La_{1-x}Mg_xMnO_3$ system, $0.05 \leqslant x \leqslant 0.4$, is proposed. Such a phase diagram summarizes a detailed study of the effects of the substitution of divalent cations of small ionic radius $\langle r_A \rangle$

at the A-sites in the manganese perovskites. Previous complementary studies of this effect—particularly in the $La_{2/3-\delta}Y_{\delta}Ca_{1/3}MnO_3$ system through the progressive replacement of La by Y at constant (optimal) Ca doping [8]—revealed that this caused a progressive depression of the temperature of the metal–insulator transition. The latter accompanied a monotonic reduction in the Mn–O–Mn bond angle below its ideal value of 180°, and associated with this was a counterintuitive drop in the corresponding hopping integral for Mn e_g electrons between adjacent, O linked, Mn ions (i.e. so-called Mn^{3+}–O–Mn^{4+} double exchange). An equivalent, more transparent view of this effect relates it to a reduction in the corresponding $Mn(e_g)$–$O(2p_\sigma)$ bandwidth with decreasing mean A-site radius $\langle r_A \rangle$ [8, 9]. Such effects are considerably more dramatic in the $La_{1-x}Mg_xMnO_3$ system where the metal–insulator transition is completely suppressed over the entire doping range studied despite the continued presence of magnetic ordering. Nevertheless, samples with the highest magnetic-ordering temperature display precursor effects of such a transition as the following results confirm.

2. Experimental details

Samples of nominal composition, $x = 0.05$, 0.1, 0.2, 0.33 and 0.4, were prepared from stoichiometric quantities of ultrapure La_2O_3, MgO (type FM) and MnO_2 (99%) using standard ceramic techniques discussed previously; the particular preheating, grinding and sintering procedures reported in [10] were adopted to maximize the magnetic-ordering temperature, an important criterion for applications considerations. Room temperature x-ray diffraction data using Cu Kα radiation were collected and analysed in the same manner as reported previously for the $x = 0.05$ specimen; these indicated a single-phased orthorhombic structure (Pbnm) with lattice constants ($c/\sqrt{2} < a < b$) summarized in table 1. The typical grain size in these polycrystalline specimens is between 30 and 40 μm.

Table 1. Lattice parameters, a measure of the distortion (ε_c), ferromagnetic ordering (T_c) and paramagnetic Curie temperatures (θ), Hopkinson maximum susceptibilities ($\chi(0, T_H)$) and effective moments (p_{eff}).

x	Lattice parameters (Å)	$\varepsilon_c = \left\|1 - \frac{c\sqrt{2}}{a+b}\right\| \times 10^3$	T_c (K)	$\chi(0, T_H)$ (emu/g Oe)	θ (K)	p_{eff} (μ_B)
0.05	$a = 5.490(7)$ $b = 5.709(7)$ $c = 7.725(4)$	25	147.2	0.13	170	6.2 (4)
0.1	5.525(6) 5.749(1) 7.714(2)	33	154.2	0.34	203	5.2 (7)
0.2	5.536(7) 5.752(4) 7.801(2)	23	139.5	0.22	187	5.1 (0)
0.33	5.530(1) 5.756(6) 7.801(7)	23	118.0	0.09	171	4.4 (0)
0.40	5.531(1) 5.720(6) 7.789(7)	21	114.8	0.16	147	4.6 (0)

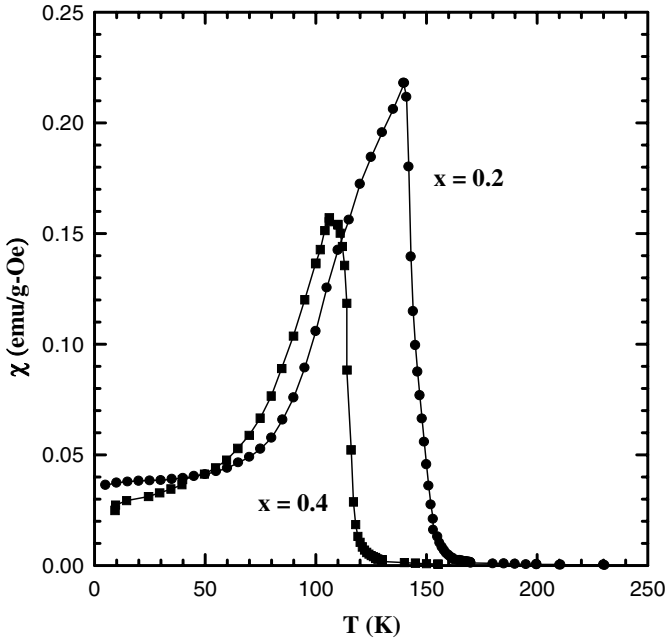

Figure 1. The zero-field ac susceptibility, $\chi(0, T)$, corrected for background and demagnetizing effects, plotted against temperature, T (K), for the $x = 0.2$ and 0.4 samples. Note the absence of any anomaly at or below 50 K, and above 170 K, as discussed in the text.

Ac susceptibility, dc magnetization and transport data were collected on samples of approximate dimensions $(1 \times 1 \times 7)$ mm^3. The magnetic data were acquired as a function of both field and temperature with a Quantum Design PPMS model 6000 system. Neither the magnetic nor the structural data indicated the presence of impurity phases—particularly Mn_3O_4 and self-doped $La_{1-y}MnO_3$ which display marked features, especially in the magnetic response [11]—confirming that the Mg ions were incorporated substitutionally for La. The transport measurements were carried out using standard four-probe techniques.

3. Results and discussion

3.1. Magnetic data

3.1.1. General features. In all the samples studied the ac susceptibility $\chi(0, T)$ increases rapidly with decreasing temperature as the ferromagnetic-ordering temperature T_c is approached from above. $\chi(0, T)$ peaks below T_c at the so-called Hopkinson (principal) maximum, and then decreases essentially monotonically with further decrease in temperature as shown in figure 1 for the $x = 0.2$ and 0.4 samples. This behaviour is generally similar to that reported previously for the $x = 0.05$ sample [10]. It is reproduced here to emphasize the absence of a signal arising either from an Mn_3O_4 impurity phase near 40 K [11] or from mixed MnMgO phases with lower ordering temperatures [12], a feature necessarily arising from Mg replacement of Mn rather than La, as well as similar signals resulting from the presence of self-doped $La_{1-y}MnO_3$ which, for $y \geqslant 0.03$, orders at or above 180 K [11, 13]. The susceptibility values—corrected for background and demagnetizing effects—at the Hopkinson peak, $\chi(0, T_H)$, are listed in table 1.

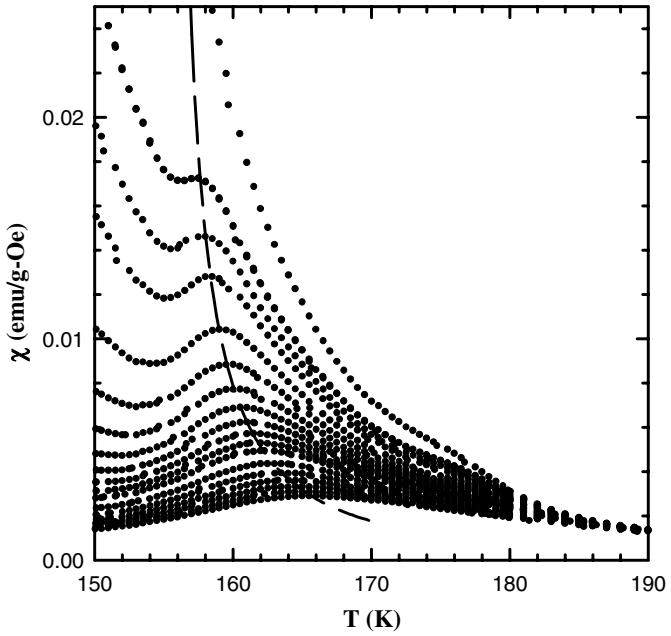

Figure 2. The ac susceptibility, $\chi(H, T)$, of the $x = 0.1$ specimen, measured in various superimposed static biasing fields from 200 (top) to 2000 Oe (bottom), plotted against temperature. The locus of the local critical maxima (the dashed curve) defines the crossover line in the (H–T) plane (see text).

3.1.2. $0.05 \leqslant x \leqslant 0.1$: nearly ideal behaviour. Figure 2 reproduces the behaviour of the ac susceptibility $\chi(H_a, T)$ of the $x = 0.1$ specimen (corrected for background and demagnetizing effects) measured in various static (dc) biasing fields, H_a, as a function of temperature near the ferromagnetic-ordering temperature T_c (both the ac driving field and the static biasing fields were applied parallel to the longest sample dimension). The static applied fields progressively suppress the Hopkinson maximum in amplitude and temperature enabling true critical peaks—shown in figure 2—to be resolved. As discussed previously for a variety of metallic and semiconducting systems [10, 14, 15], these critical peaks move upward in temperature away from T_c and decrease in amplitude as H_a is increased. The locus of these peaks in the (H–T) plane defines the crossover line above which the response is thermally controlled while below this line it is field-dominated [16]. The general behaviour of this peak structure can be understood on both the basis of the fluctuation-dissipation theorem [16] and through numerical calculations for the ferromagnetic phase of Sherrington–Kirkpatrick-like (SK) models [17]. Since a detailed analysis of the peak behaviour on the basis of the scaling law equation of state to extract estimates for the usual critical exponents γ, β and δ has been thoroughly discussed previously [10, 14, 15, 18]; its principal conclusions alone are summarized below:

(i) The critical peak amplitude $\chi(H_i, T_m)$ is predicted to exhibit a power-law dependence on the internal field ($H_i = H_a - NM$, in the usual notation), namely

$$\chi(H_i, T_m) \propto H_i^{1/\delta - 1}. \tag{1}$$

Such a relationship enables estimates for δ to be made *independent of the choice or knowledge of* T_c. This procedure is illustrated in figure 3(a) in which the critical peak

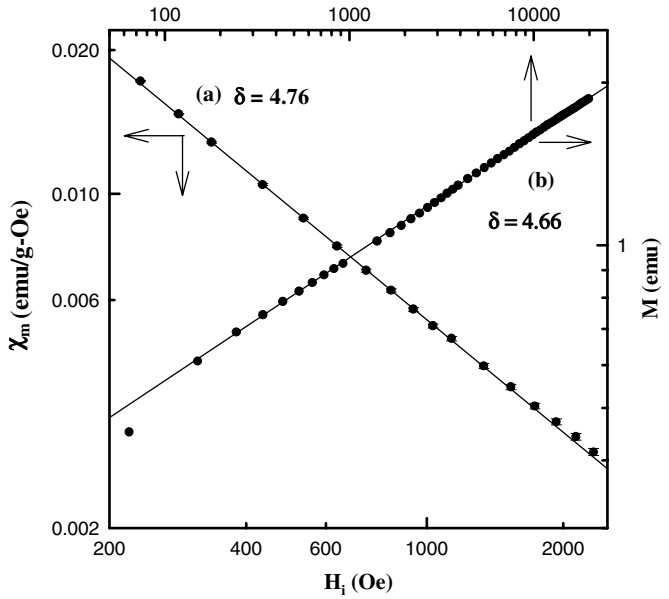

Figure 3. (a) The amplitude of the critical maxima $\chi_m = \chi(H_i, T_m)$, for the $x = 0.1$ sample taken directly from figure 2, plotted against the internal field H_i (in Oe) on a double logarithmic scale. The straight line drawn confirms the power-law prediction (equation (1)) and its slope yields $\delta = 4.76$. (b) The magnetization M of the same sample measured along the critical isotherm and displayed against H_i on a double logarithmic plot; the straight line drawn yields $\delta = 4.66$.

amplitudes taken directly from figure 2 are plotted against the estimated internal field H_i (the demagnetization factor N being found from the slope of the M versus H_a plots near T_c—the 'shearing' curve) on a double logarithmic scale. The ensuing straight line confirms the power-law prediction of equation (1) and a least-squares fit yields a slope from which the value for δ is found to be

$$\delta = 4.75 \pm 0.15 \qquad 200 \lesssim H_i \lesssim 2\,\text{kOe}.$$

(ii) This same approach relates the temperature T_m of the critical peak maxima (also taken directly from figure 2) to the internal field via

$$\frac{T_m - T_c}{T_c} = t_m \propto H_i^{(\gamma+\beta)^{-1}}. \tag{2}$$

A test of this relationship is implemented by first plotting T_m against $H_i^{(\gamma+\beta)^{-1}}$, with the projected intercept at $H_i = 0$ yielding an estimate[1] for T_c of 154.5 ($\pm$0.5 K). The latter is then used to construct a double logarithmic plot of t_m versus H_i (figure 4). The least-squares fitted straight line drawn in this figure confirms the power-law prediction of equation (2) and yields

$$\gamma + \beta = 1.75 \pm 0.10 \qquad 200 \leqslant H_i \leqslant 2\,\text{kOe}.$$

[1] This procedure should yield a straight line (provided, of course, that the correct exponent values are utilized), so the extrapolation is straightforward. Small adjustments ΔT_c in T_c are admitted ($\Delta T_c/T_c \simeq 2$–4×10^{-3}) until consistent sets of plots are achieved. A range of possible exponent values are also tested.

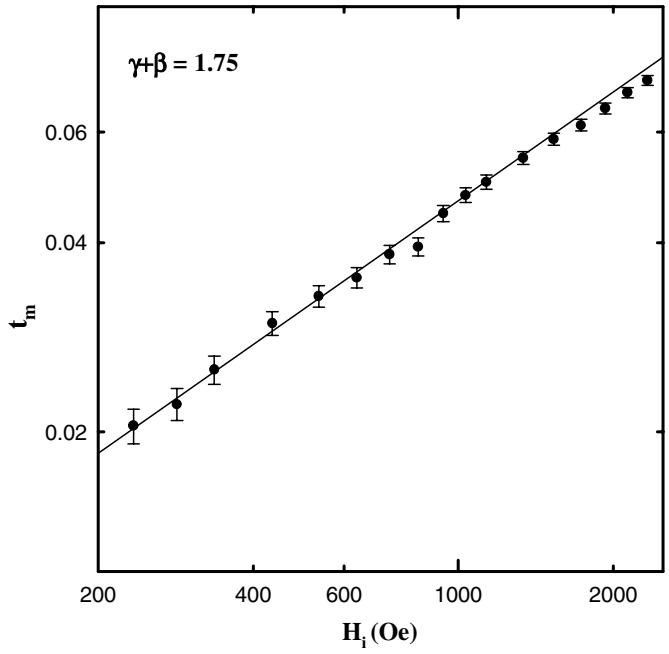

Figure 4. The (reduced) critical peak temperature, t_m, taken from figure 2 for the $x = 0.1$ specimen and plotted against the internal field H_i (in Oe) on a double logarithmic scale. The straight line drawn confirms the power-law prediction of equation (2) and its slope yields $\gamma + \beta = 1.75$.

(iii) Finally, the same value for T_c is utilized to test a third power-law prediction, namely

$$\chi(H_i,\ T_m) \propto t_m^{-\gamma}. \tag{3}$$

Figure 5—a double logarithmic plot of the critical peak amplitudes (again taken directly from figure 2) against the reduced peak temperature t_m (also evaluated directly from the same figure)—summarizes the results of such an analysis. The least-squares fitted line confirms the power-law relationship and yields

$$\gamma = 1.39 \pm 0.05 \qquad t_m \gtrsim 3 \times 10^{-2}.$$

These exponent values are, within experimental uncertainty, in agreement with those predicted by the nearest-neighbour, isotropic three-dimensional Heisenberg model [19] ($\delta = 4.80$, $\gamma + \beta = 1.75$, $\gamma = 1.38(6)$). They are in excellent agreement with those reported earlier for an $x = 0.05$ specimen [10], but, more importantly, they indicate that the regime where near-ideal magnetic behaviour is observed (that is, exponent values not only falling into the universality class of a well-established model system but also maintained over the entire range of field and (reduced) temperature examined) extends to $x = 0.1$ in this system.

The exponent value estimates satisfy the Widom relation, $\gamma = \beta\,(\delta - 1)$, and the δ estimate is confirmed by measurements along the critical isotherm $\left(M \propto H_i^{1/\delta}; \delta = 4.66 \pm 0.15\right.$ for $500 \leqslant H_i \leqslant 20$ kOe, figure 3(b)), although this estimate *is* dependent not only on the estimated value for T_c but also on the reliability of both resetting and remeasuring at this same temperature. The scaling law approach also predicts that the susceptibility $\chi(h, t)$ measured in any fixed field and normalized to its peak value (in the same field) should be a universal function of the argument of the scaling function, namely

$$\frac{\chi(h,t)}{\chi(h,t_m)} \propto \frac{t}{H_i^{(\gamma+\beta)^{-1}}}.$$

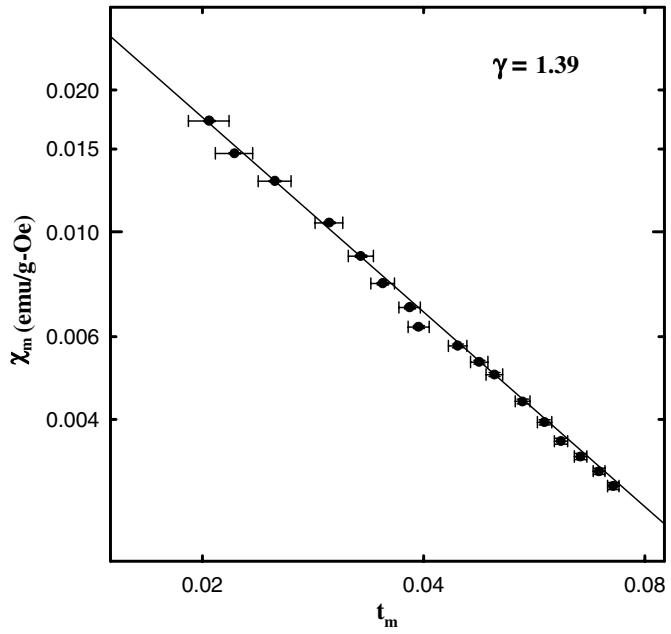

Figure 5. The critical peak amplitude, $\chi_m = \chi(H, T_m)$, taken directly from figure 2 for the $x = 0.1$ specimen and plotted against the reduced critical peak temperature, t_m, taken from the same figure, on a double logarithmic scale. The line drawn confirms the power-law prediction of equation (3) and its slope yields $\gamma = 1.39$.

The above data on the $x = 0.1$ specimen collapse onto a single-scaling curve using Heisenberg model exponents, i.e. $(\gamma + \beta)^{-1} = 0.57$. Since a figure of the latter type is similar to that presented previously for the $x = 0.05$ sample [10, 20], it is not reproduced here.

3.1.3. $0.1 < x \leqslant 0.33$: concentration dependent effects. Figures 6 and 7 for the $x = 0.2$ sample are the equivalent of the last three figures presented above for the $x = 0.1$ specimen. A comparison of the two sets of figures enables the effects of increased divalent cation substitution to be assessed.

Figure 6(a)—a double logarithmic plot of the critical peak maxima, $\chi(h, t_m)$, against the internal field, H_i—shows that the power-law prediction of equation (1) is no longer valid over the entire field range. This plot now exhibits some curvature so that the *effective* exponent $\delta^*(H_i)$—determined from the *local* slope $\partial \ln \chi(H_i, T_m)/\partial \ln H_i$ of this plot—*decreases* with increasing field. The line drawn in this figure, a least-squares fit of the five points at lowest field, yields

$$\delta = 4.76 \pm 0.20$$

suggesting that the *asymptotic* (low-field) value for this exponent is still consistent with the 3D Heisenberg model prediction. Fitting the entire data set shown in this figure yields a somewhat lower effective/average exponent value of

$$\delta^* = 4.43 \pm 0.23.$$

Effective exponent values which vary with field and/or temperature have been reported previously for a variety of metallic and semiconducting systems [14, 21, 22]. An extensive

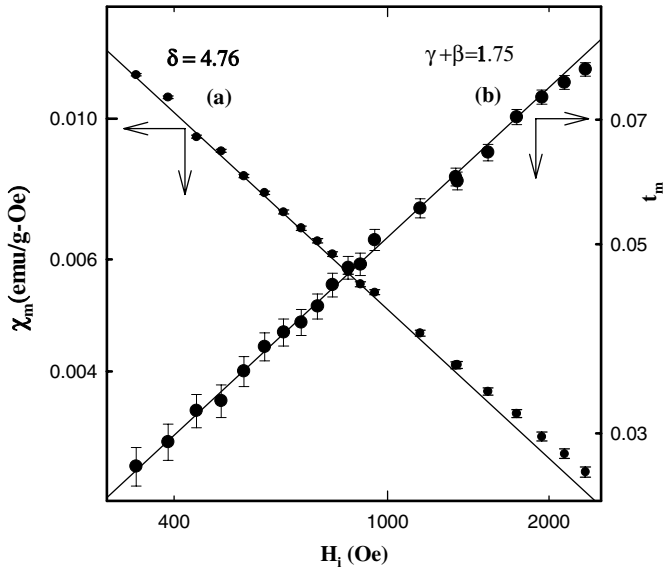

Figure 6. (a) As in figure 3(a), for the $x = 0.2$ sample. The solid line drawn—a fit to the first five points—yields $\delta = 4.76$. See text for further discussion. (b) As in figure 4, for the $x = 0.2$ specimen.

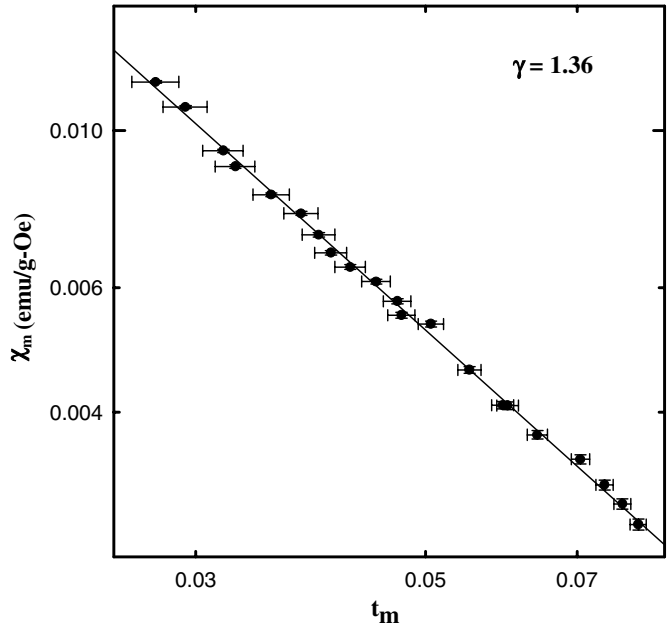

Figure 7. As in figure 5, for the $x = 0.2$ sample.

study of metallic systems has led to the conclusion that this variation is linked to a finite width in the distribution of exchange interactions coupling the spins (the Mn moments here). Further, while such 'disorder' has been shown to be an irrelevant scaling field *at* the critical point, so

that the *asymptotic* ($h \to 0, t \to 0$) exponent values remain unchanged (in agreement with the Harris criterion [23]), the *effective* exponent values (for $h \neq 0, t \neq 0$) are modified by its presence. This modification becomes more pronounced as the ratio $\eta = J_0/J$ (where J_0 is the mean value/first moment of the exchange distribution and controls the critical temperature, $k_B T_c = J_0$, while J measures the width/second moment) is reduced towards 1.0 (essentially the limit of stability of a ferromagnetic ground state). Similar effects can be seen in figures 6(b) and 7, which also show effective exponent values that vary with field and/or temperature, but with *low* field/temperature (i.e. asymptotic) exponent values consistent with the same model predictions, namely

$$\gamma + \beta = 1.75 \pm 0.15 \qquad \gamma = 1.36 \pm 0.04.$$

Results for the $x = 0.33$ sample are very comparable; specifically, they are very similar in the trends in the effective exponent values to those found above and to earlier measurements [24] at this composition ($x = 0.33$), despite the fact that the annealing procedure adopted here has elevated T_c appreciably.

The physical picture that emerges therefore in this composition range ($0.1 \leqslant x \leqslant 0.33$) is that increased divalent cation substitution for La leads to an increase in the width (J) of the distribution of exchange coupling strengths between Mn spins (although the first moment J_0 is still relatively large, so that $\eta \gg 1$). In a double exchange picture this has a clearly identifiable origin—the presence of an inhomogeneous mixed valent (Mn^{3+}, Mn^{4+}) state. Within the latter, the presence of ferromagnetic Mn^{3+}–Mn^{4+} double exchange along with both Mn^{3+}–Mn^{3+} and Mn^{4+}–Mn^{4+} (superexchange) interactions of different magnitudes (and probably sign) would lead to a progressively broadened exchange coupling distribution as the doping level increases. Nevertheless ferromagnetism predominates so that η remains >1. (In fact, close examination of figures 3–5 for the $x = 0.1$ specimen indicates that such effects might be manifest at the highest fields used there.) These effects are likely clearer and more pronounced at higher values for x, as discussed next.

3.1.4. $x = 0.4$. Figures 8 and 9 summarize the attempts to assess the validity of the power-law predictions, equations (1)–(3), and the associated exponent values at still higher substitution levels. This analysis yields the surprising result that while these power laws fit the available data over the entire field and temperature range examined ($200 \leqslant H_i < 2.2$ kOe; $1.6 \times 10^{-2} \leqslant t_m < 8 \times 10^{-2}$), they do so with (effective) exponent values quite different from those found at lower values of x; that is, figures 8 and 9 yield

$$\delta^* = 3.0 \pm 0.1 \qquad \gamma^* + \beta^* = 1.49 \pm 0.11 \qquad \gamma^* = 1.01 \pm 0.06.$$

These values are close to those predicted in the mean field ($\gamma = 1$, $\gamma + \beta = 3/2$, $\delta = 3$), an unexpected result considering the basic (and short-range) nature of the interactions believed to be prevalent in these systems—double- and superexchange. Two possibilities present themselves. First, there is a fundamental change in the character of the basic interaction mechanism as the divalent cation substitution increases from $x = 0.33$ to 0.40. For $x \leqslant 0.33$ the estimated exponents appear to be consistent with the predictions of the *near-neighbour* 3D Heisenberg model; at $x = 0.40$ the range of the underlying interactions becomes infinite. Such a change would indeed be very marked. Alternatively, the trend evident for $0.2 \leqslant x \leqslant 0.33$ continues; that is, the ratio $\eta = J_0/J$ continues to fall towards unity, with the extent of the regime in the (h, t) plane within which true *asymptotic* critical behaviour is observed contracting *below* the field and temperature range accessed by the present experiment. The current experiment suffers some of the same limitations as conventional estimates of static critical exponents from magnetization measurements. Neither can be extended to arbitrarily

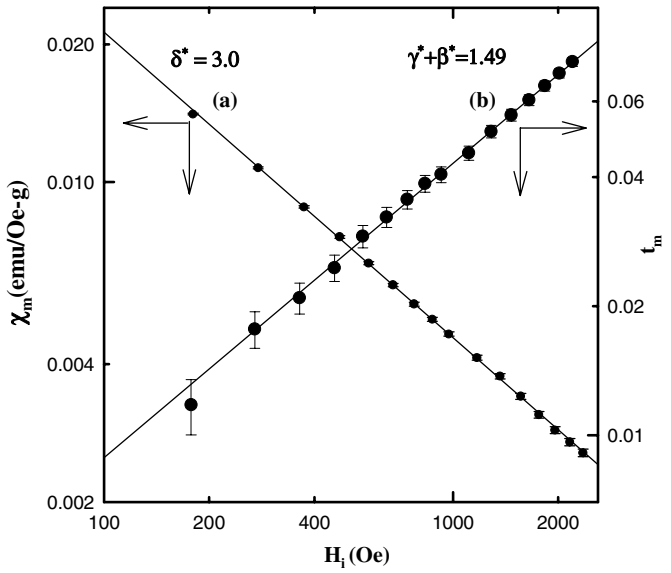

Figure 8. (a) As in figure 3(a), for the $x = 0.4$ sample. The δ-value is discussed in the main text. (b) As in figure 4, for $x = 0.4$.

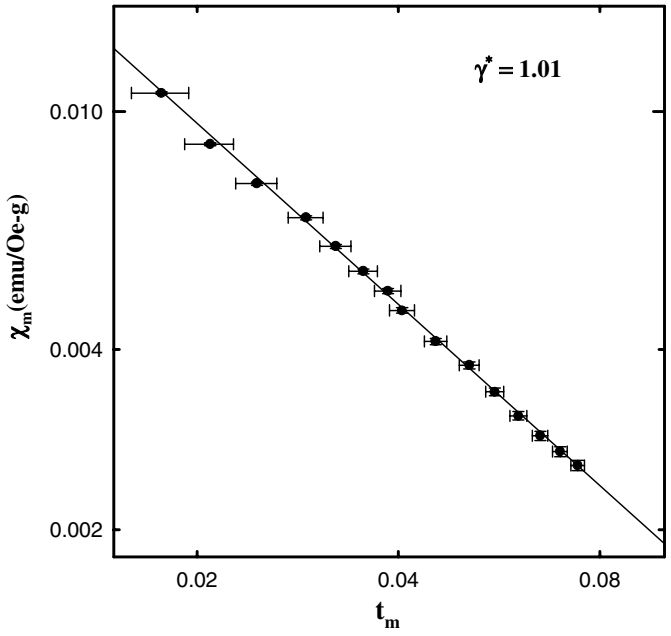

Figure 9. As in figure 5, for $x = 0.4$.

low field/(reduced) temperature due to complications introduced by the presence of regular, i.e. non-critical, contributions in the total magnetic response [10] (arising typically from such sources as domain wall motion and/or coherent rotation). The latter limit the current measurements to internal fields down to 200 Oe (somewhat lower than those *typically* accessed in the corresponding magnetization based approaches). The true critical behaviour may thus

prove very difficult to assess. Further, while it is well established that *effective* exponent values tend towards mean-field predictions away from the critical point, such a trend generally occurs in a more gradual way than that seen above. Specifically, if this second proposal is correct, the true critical region contracts very rapidly for $x > 0.33$ in $La_{1-x}Mg_xMnO_3$, which reflects a rapid decline in the ratio $\eta = J_0/J$ towards unity as the dopant levels increase above this composition.

While the present measurements do not differentiate between these two possibilities, we currently favour the second on the basis of preliminary measurements made at yet higher values of x. In particular, if $\eta \leqslant 1.0$ one would expect the ground state to evolve into a spin glass, and for $1.0 < \eta \leqslant 5/4$ so-called re-entrant (paramagnetic to (longitudinal) ferromagnetic to (transverse) spin-glass ordering) behaviour is predicted by various model approaches [14, 25]. The preliminary measurements available for $0.45 \leqslant x \leqslant 0.6$ display features *superficially* reminiscent of those associated with the second possibility. However, more detailed investigations currently underway of both the linear and nonlinear responses are necessary before firm conclusions can be drawn at these compositions. Despite the need for the latter, the present measurements of the low-field (linear) response indicate the presence of some unusual features at temperatures below T_c; these are discussed next.

3.1.5. Field-cooled (FC) and zero-field cooled (ZFC) magnetizations. Figures 10(a)–(d) reproduce the field-cooled (FC) and zero-field cooled (ZFC) magnetizations of the four samples with x between 0.1 and 0.4 in an applied field of 10 Oe. While the FC data are relatively featureless, the ZFC branch exhibits a sharp decline at a temperature which decreases with increasing x (from about 90 K for $x = 0.1$ to near 60 K for $x = 0.4$). Figures 11(a)–(d) display the temperature dependences of the corresponding coercive fields, $H_c(T)$, deduced from magnetization curves at various temperatures. In general, the decline in the ZFC branch corresponds to the temperature at which $H_c(T)$ displays its most rapid increase (or, at least, the onset of a rapid increase). These features are very similar to those reported earlier for the $x = 0.05$ specimen, and can be modelled using the same Preisach-based approach used there [10, 26]; such fits are shown representatively for the $x = 0.1$ sample in figure 10(a). The principal feature emerging from this type of fit is that these data can be modelled by a coercive field that exhibits a (model-generated) increase in $H_c(T)$ with decreasing temperature which is significantly more pronounced than that actually measured; figure 11(a) reproduces this comparison for the $x = 0.1$ sample. The features displayed by the data in figures 10 and 11, as well as the characteristics of the model $H_c(T)$ distribution, warrant further comment.

While the Preisach model provides a good overall representation of these data ([10] provides such a comparison more comprehensively), this model is phenomenological in nature [27]. Specifically, it does not identify the underlying mechanism leading to the rapid decrease (increase) in the ZFC data ($H_c(T)$) with decreasing temperature. Since this model has been applied explicitly to hysteretic processes, it might be argued that the features discussed above are intrinsically technical in nature, that is, they may not be linked with a true thermodynamic phase change. This contention cannot be demonstrated conclusively by data currently available. Consequently, a phase diagram for this system has been constructed (figure 12) which includes the possibility of some characteristic property undergoing significant modification at a temperature determined by the rapid decline in the ZFC branch of the low-field magnetization. A candidate for such an effect might be spontaneous (inhomogeneous) electronic phase separation [5, 28], which is discussed in more detail below. This feature is shown by the dashed curve in figure 12.

In contrast, the solid curve at higher temperatures designates the ferromagnetic-ordering temperatures, T_c, estimated in the manner discussed in sections 3.1.2–3.1.4, and associated

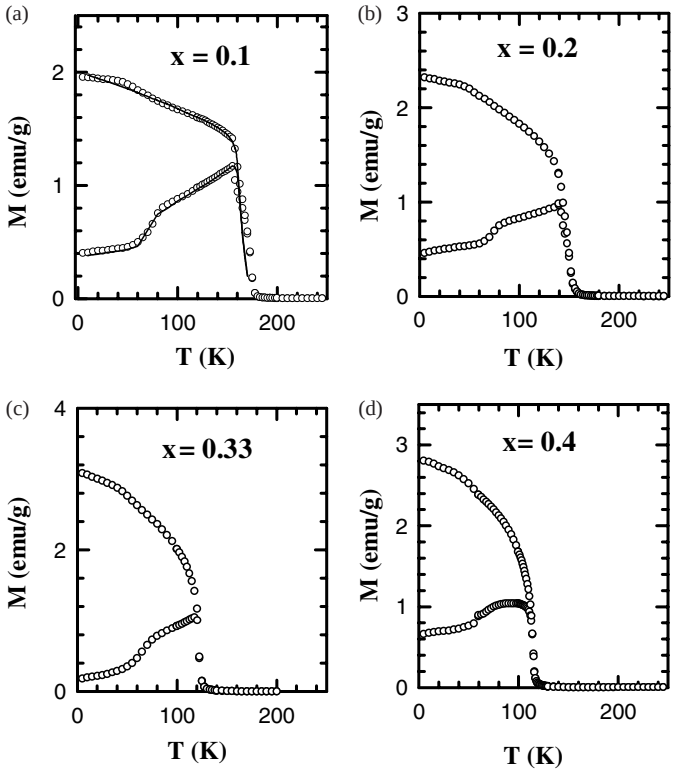

Figure 10. The zero-field cooled (lower) and field-cooled magnetizations M (in emu g^{-1}) measured in an applied field of 10 Oe and plotted against temperature for (a) $x = 0.1$, (b) $x = 0.2$, (c) $x = 0.33$ and (d) $x = 0.4$. The solid curve in (a) is a fit to the Preisach model discussed in the text.

unequivocally with a thermodynamic transition. The characteristics of this phase diagram are, however, incomplete without the following discussion.

3.2. Transport data

Resistivity data in zero field and an applied field of 1.5 T were collected at and below room temperature. However, since all the specimens examined remained semiconducting, their continuing increase in resistivity $\rho(T)$ with decreasing temperature precluded measurements being carried out below about 90 K. Nevertheless, some qualitative differences in the transport behaviour of these samples occur with changes in x, which complicates a quantitative analysis of this behaviour in some cases (specifically for $x = 0.1$ and 0.2 at temperatures below T_c). This is illustrated in figures 13 and 14. Figure 13 shows the zero-field resistivity $\rho(T)$ for the $x = 0.4$ specimen; here $\rho(T)$ increases monotonically with decreasing temperature with no anomaly in $\rho(T)$ or its derivative at T_c. Such behaviour is found for $x = 0.05$ [20], 0.33 and 0.40. Figure 14 reproduces the $\rho(T)$ versus T behaviour at $x = 0.2$; here $d\rho/dT$ is anomalous, displaying a maximum in the vicinity of T_c, although this derivative remains negative. The situation at a true metal–insulator transition, where the transition temperature is frequently identified as the maximum in this derivative, is that this latter derivative becomes positive. The results reported here are precursor effects to such a transition. A similar result is observed at $x = 0.1$. Such behaviour is reminiscent of the $La_{1-x}Sr_xMnO_3$ system at similar doping levels

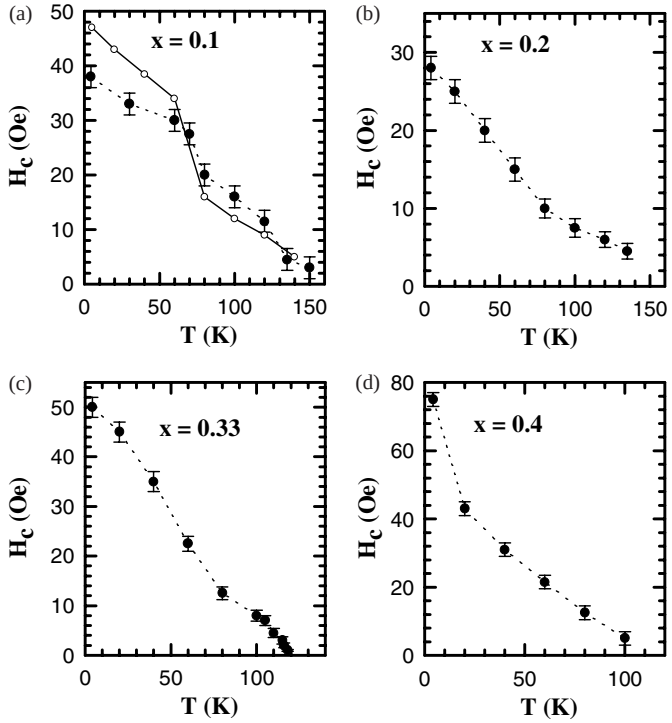

Figure 11. The measured temperature dependence of the coercive field, $H_c(T)$ (in Oe), for (a) $x = 0.1$, (b) $x = 0.2$, (c) $x = 0.33$ and (d) $x = 0.4$. The dashed curves are guides for the eye, while the open symbols joined by a solid curve are derived from the Preisach model fit to the data in figure 11(a).

[29]. In this latter system, however, further increases in x ($\geqslant 0.175$) cause T_c to increase, with the associated emergence of a metal–insulator transition. By contrast, in $La_{1-x}Mg_xMnO_3$, increasing x beyond 0.1–0.2 causes T_c to fall (T_c is a maximum in this system near $x \sim 0.1$), resulting in the transport behaviour reverting to the monotonic semiconducting response seen for $x < 0.1$. This is an intriguing difference with both the $La_{1-x}Sr_xMnO_3$ and $La_{1-x}Ca_xMnO_3$ systems, a situation which—as discussed in section 1—likely arises due to influence of the average A-site radius on the Mn e_g–O($2p_\sigma$) bandwidth (and the associated Mn–O–Mn bond angle); an interesting corollary to this might be that an increase in T_c and the appearance of a metal–insulator transition might be induced by the application of pressure in $La_{1-x}Mg_xMnO_3$ for $0.1 \leqslant x \leqslant 0.2$.

To turn next to a quantitative analysis of these data, the resistivities $\rho(T)$ in the semiconducting regimes both above and below T_c have been fitted to the expression

$$\rho(T) = \rho_0 T^n e^{E_a/k_B T}. \tag{4}$$

With $n = 1$ or $3/2$, such an expression represents charge transport by polaronic hopping in the adiabatic or non-adiabatic regime, respectively [30], while equation (4) with $n = 1$ has also been proposed recently as a form appropriate for the resistivity of non-metallic phase-separated manganites containing small magnetic polarons [31]. In the latter, transport is accomplished by electron transfer *between* polarons rather than by the field-induced movement of the polaronic entities themselves. The various scenarios covered by equation (4) with either choice for n thus appear to include those models currently regarded as most appropriate for discussing transport

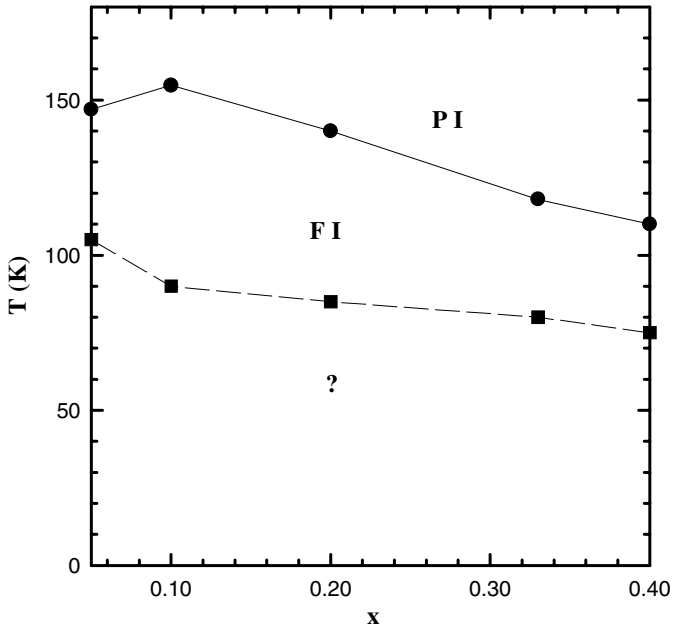

Figure 12. The suggested phase diagram for the $La_{1-x}Mg_xMnO_3$ system. PI: paramagnetic insulator; FI: ferromagnetic insulator. The upper temperatures represent the measured T_cs while the lower 'boundary' is discussed in the text.

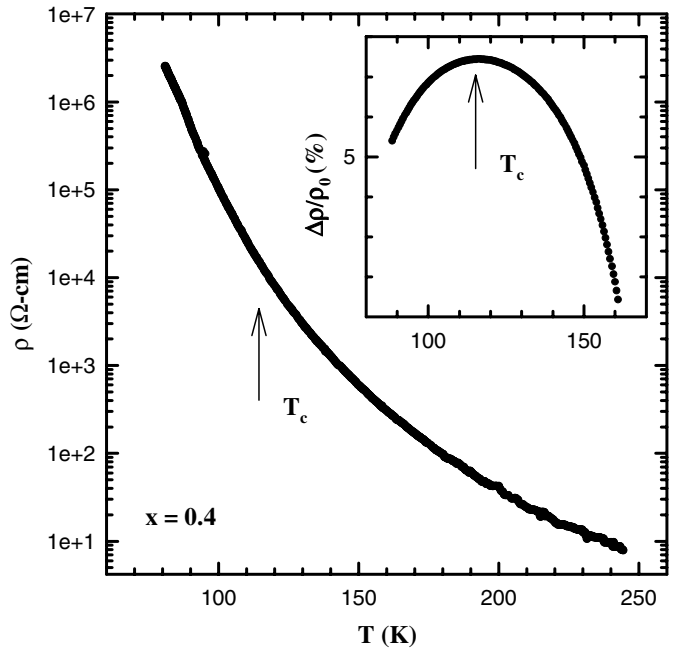

Figure 13. The zero-field resistivity, $\rho(T)$ (in Ω cm), plotted on a logarithmic scale against temperature, T (in K), for the $x = 0.4$ sample. The inset shows the fractional magnetoresistance $\Delta\rho/\rho$ (in %) measured in an applied field of 1.5 T.

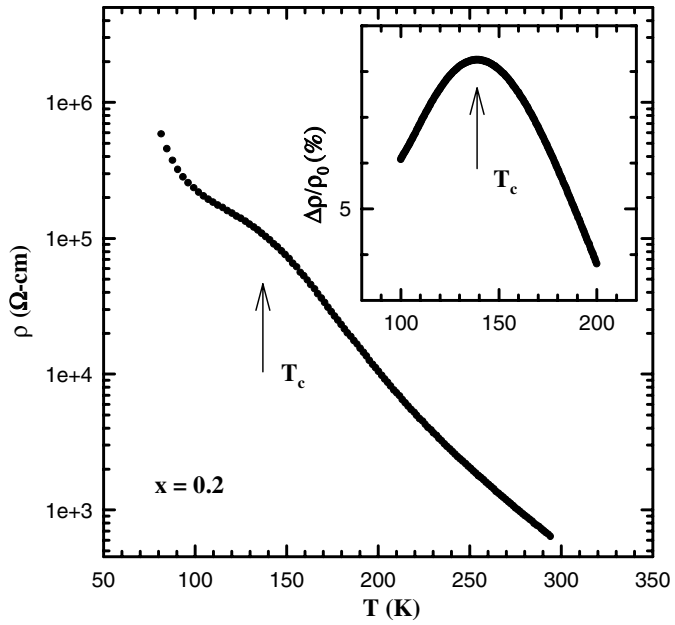

Figure 14. As in figure 13, for $x = 0.2$.

behaviour in doped manganese perovskites. (Recent numerical calculations for mixed-phased manganites [32] can also replicate experimental data but, being non-analytical in form, cannot be compared directly with current measurements. Furthermore, a recent model [33] in which phase separation is modelled by co-existing metallic and insulating regions with the resistivity of the latter given by equation (4) with $n = 1$ essentially assumed a form for ρ_0 consistent with equation (5), so subsequent discussion is also consistent with it.)

Figure 15 reproduces representative fits of equation (4) to the transport data; figure 15(a) illustrates a fit of the 'adiabatic' form ($n = 1$) to the $x = 0.33$ specimen for $T > T_c$, and figure 15(b) the non-adiabatic form ($n = 3/2$) to the $x = 0.4$ sample for $T < T_c$. The corresponding least-squares fitted values for ρ_0 and the activation energy E_a are provided in table 2. As can be seen from this table, both forms of equation (4) (i.e. with $n = 1$ or $3/2$) provide equally acceptable fits to these data, as has been found in other systems [30], however, based on the internal consistency of model parameters, definite conclusions can be drawn. In the often utilized adiabatic limit the parameter ρ_0 can be written as [30, 34]

$$\rho_0 = \frac{k_B a}{g_d x(1-x) e^2 \Omega_0}. \tag{5}$$

Here the hopping distance a is identified with the nearest-neighbour Mn separation, g_d is a numerical factor ($\geqslant 1$) characterizing the topology of the hopping processes and Ω_0 is an attempt frequency, identified with a characteristic longitudinal optical phonon frequency, ω_0, in this limit. The factor $x(1-x)$ reflects (single) site occupation effects (arising from on-site Coulomb repulsion), x being the hole/Mn^{4+} fraction. In the non-adiabatic regime the prefactor is modified slightly, becoming [34]

$$\rho_0 = \frac{k_B a}{x(1-x)e^2\Omega_0}\frac{1}{T^{1/2}} = \frac{k_B a}{x(1-x)e^2}\frac{\hbar}{J^2}\left[\frac{4E_a k_B}{\pi}\right]^{1/2} \tag{6}$$

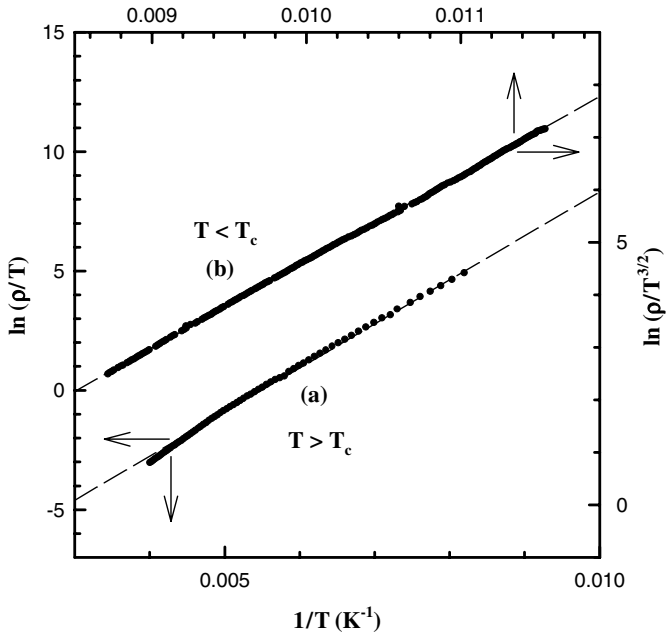

Figure 15. (a) A fit of the data above T_c for $x = 0.33$ to the adiabatic formalism (equation (4) with $n = 1$). (b) A fit of the data below T_c for $x = 0.4$ (figure 13) to the non-adiabatic form (equation (4) with $n = 3/2$).

Table 2. Parameters deduced from transport data.

	$T > T_c$						$T < T_c$					
	Adiabatic ($n = 1$)			Non-adiabatic ($n = 3/2$)			Adiabatic ($n = 1$)			Non-adiabatic ($n = 3/2$)		
x	E_a (meV)	ρ_0 (Ω cm)	SE	E_a (meV)	ρ_0 (Ω cm)	SE	E_a (meV)	ρ_0 (Ω cm)	SE	E_a (meV)	ρ_0 (Ω cm)	SE
0.05	139	7.8×10^{-6}	0.014	171	3.1×10^{-7}	0.012	116	1.6×10^{-4}	0.049	121	9.2×10^{-6}	0.054
0.10	176	1.7×10^{-4}	0.033	186	6.5×10^{-6}	0.036	—	—	—	—	—	—
0.2	176	2.3×10^{-3}	0.034	192	6.8×10^{-5}	0.025	—	—	—	—	—	—
0.33	192	6.5×10^{-6}	0.004	202	2.8×10^{-7}	0.004	135	3.6×10^{-4}	0.017	140	2.1×10^{-5}	0.021
0.4	160	1.8×10^{-5}	0.093	165	9.7×10^{-7}	0.091	116	1.2×10^{-3}	0.047	123	8.4×10^{-5}	0.054

an expression which is valid when

(i) the electronic coupling factor/transfer matrix element $J \ll$ polaron formation energy (related, but not equal, to E_a) and

(ii) $$\Omega_0 = \frac{J^2}{\hbar}\left[\frac{\pi}{4E_a k_B T}\right]^{1/2} \ll \omega_0. \tag{7}$$

In both situations the characteristic frequency $\omega_0 \simeq 10^{13}$–10^{14} Hz [34, 35].

Finally, in the phase-separation scenario of [31]

$$\rho_0 = \frac{k_B}{128\pi e^2 \nu_0 n^2 \ell^5} \tag{8}$$

where n is the polaron density (equated with the carrier/hole density induced by doping), ν_0 is a characteristic magnon frequency and ℓ is a tunnelling length. Rakhmanov *et al* [31] estimate ν_0 to be on the order of the Fermi energy inside polarons, finding $\nu_0 \simeq 4 \times 10^{13}$ Hz $\simeq \omega_0$ (above).

Using equations (6)–(8) with the listed values for ρ_0 enables estimates for the parameters Ω_0 and ℓ to be made and compared with model assumptions. These estimates are summarized in table 3. An examination of the values for ℓ so derived indicate that the phase-separation model, as formulated by Rakhmanov *et al* [31], is inconsistent with the current data. These yield $\ell < 1$ Å, significantly smaller than both the Mn nearest-neighbour separation (∼3.9 Å) and the inequality on which the model expression is predicated, that is, $\ell > 2\ a_0$, a_0 being the polaron radius, estimated to be around 10 Å [36]. Further, while transport data were not acquired below 90 K (for reasons outlined previously), there are no indications of a fall in $\rho(T)$ at lower temperatures, specifically on crossing the lower (tentative) boundary of the phase diagram (figure 12).

Table 3. Model parameters.

	$T > T_c$				$T < T_c$			
	Adiabatic/phase separation		Non-adiabatic		Adiabatic/phase separation		Non-adiabatic	
x	Ω_0	ℓ (Å)	Ω_0	$\|J\|$(meV)	Ω_0	ℓ (Å)	Ω_0	$\|J\|$ (meV)
0.05	6×10^{13}	0.7	9×10^{13}	—	3×10^{12}	0.4	4×10^{12}	11
0.1	1.5×10^{12}	0.4	2.5×10^{12}	10	—	—	—	—
0.2	6×10^{10}	0.2	10^{11}	2.5	—	—	—	—
0.33	1.5×10^{13}	0.9	2.5×10^{13}	—	3×10^{11}	0.2	5×10^{11}	3.5
0.4	5×10^{12}	0.7	6×10^{12}	16	4×10^{10}	0.3	10^{11}	1.5

Nevertheless, this boundary has been retained, albeit that it might simply represent changes in the technical magnetic properties of this system, as comparisons with specific phase-separation predictions are currently very limited. This has been done despite a recent analysis [33] suggesting that such a separation might occur *above* rather than below T_c for the small $\langle r_A \rangle$ samples studied here. The latter model is consistent, however, with the predominance of semiconducting behaviour described by equations (4) and (5) in these same small $\langle r_A \rangle$ samples, as observed here.

As far as polaronic models are concerned, in all those cases where fits to equation (4) *below* T_c were possible, the estimates for Ω_0 indicate the applicability of the *non*-adiabatic regime ($\Omega_0 \ll \omega_0 \sim 10^{13}$–$10^{14}$ Hz). In the paramagnetic regime above T_c, however, there is considerably more variance; for $x = 0.05$ [20] and 0.33 the adiabatic model appears to apply ($\Omega_0 > 10^{13}$ Hz) whereas for $x = 0.1$, 0.2 and 0.4 the non-adiabatic limit prevails. Estimates for the coupling constant J can be made using equation (6) and the tabulated ρ_0 and E_a values when the latter limit applies. Such estimates fall in the range $|J| \sim 1.5$–15 meV, comparable

to estimates for $LaMnO_3$, $LaCrO_3$ and O-depleted $La_{0.67}Ca_{0.33}MnO_{3-\delta}$ [34, 37] where the non-adiabatic regime is also operative.

Despite the above differences in the limits applicable to the behaviour of these samples in the high-temperature paramagnetic regime, the present measurements nevertheless indicate that polaronic models can describe the behaviour of hole-doped $La_{1-x}Mg_xMnO_3$ both above and below T_c. This confirms the consensus of current results for the paramagnetic phase (where both adiabatic [30] and non-adiabatic [34] regimes have been deemed applicable, depending on the system), as well as recent analyses on the ferromagnetic, *metallic* phase of $La_{1-x}Ca_xMnO_3$ films ($x = 0.2$, 0.25 and 0.4) [38]. What is unusual about the present measurements, however, is not that the activation energy E_a falls on entering the order phase (although the inequality $|J| \ll E_a$, necessary for the formation of small polarons, remains valid), but that ρ_0 increases sharply (leading to a marked decrease in Ω_0) in the ferromagnetic phase. This is, of course, necessary if E_a decreases and the resistivity changes smoothly through T_c, as is the case here. This observation conflicts with the predictions of Emin and Liu [30] that *ferromagnetic* ordering should have a minor effect on the magnitude and temperature dependence of the small polaron jump rate. It has been tentatively proposed [37] that bipolaron formation—specifically triplet pairing—*might* cause such an effect, and indeed the observation of a moderate rather than a colossal magnetoresistance that peaks near T_c (insets in figures 13 and 14) is consistent with such pairing [20, 37]. However, bipolaron formation is still far from well established in these systems, the response of which continues to pose fundamental questions half a century after their discovery.

Acknowledgments

Support for this work from the Natural Sciences and Engineering Research Council (NSERC) of Canada and the University of Manitoba is gratefully acknowledged.

References

[1] Ramirez A P 1997 *J. Phys.: Condens. Matter* **9** 8171
[2] Kaplan T A and Mahanti S D 1999 *Physics of Manganites* (New York: Plenum)
[3] Radaelli P G, Cox D E, Marezio M and Cheng S-W 1997 *Phys. Rev.* B **55** 3015
Ramirez A P *et al* 1996 *Phys. Rev. Lett.* **76** 3188
Mori S, Chen C H and Cheong S-W 1998 *Nature* **392** 473
[4] Murakami Y *et al* 1998 *Phys. Rev. Lett.* **81** 582
[5] Moreo A *et al* 1999 *Science* **283** 2034
Moreo A *et al* 2000 *Phys. Rev. Lett.* **84** 5568
Hennion M *et al* 1998 *Phys. Rev. Lett.* **81** 1957
[6] Alonso J A *et al* 1999 *Phys. Rev. Lett.* **82** 189
Harris M J *et al* 1998 *Phys. Rev. Lett.* **81** 4496
[7] Schiffer P, Ramirez A P, Bao W and Cheong S-W 1995 *Phys. Rev. Lett.* **75** 3336
Tomioka Y, Asamitsu A, Kuwahara H, Moritomo Y and Tokura Y 1996 *Phys. Rev.* B **53** R1689
[8] Fontcuberta J, Martinez B, Seffar A, Piñol S, Garcia-Muñoz J L and Obarados X 1996 *Phys. Rev. Lett.* **76** 1122
[9] Frontera C *et al* 2001 *J. Phys.: Condens. Matter* **13** 1071
[10] Zhao J H *et al* 2000 *J. Phys.: Condens. Matter* **12** 6903
Zhao J H *et al* 2001 *J. Appl. Phys.* **89** 7248
[11] de Brion S *et al* 1999 *Phys. Rev.* B **59** 1470
Dwight K and Menyuk N 1960 *Phys. Rev.* **119** 1470
[12] Jacobs I S and Kouvel J S 1961 *Phys. Rev.* **122** 412
[13] Kang J S *et al* 2001 *J. Phys.: Condens. Matter* **13** 3779
[14] Williams G 1991 *Magnetic Susceptibility of Superconductors and Other Spin Systems* ed R A Hein *et al* (New York: Plenum) p 475 ff

[15] Zhao J H *et al* 1999 *Phys. Rev. Lett.* **83** 219
Wang Z, Kunkel H P and Williams G 1992 *J. Phys.: Condens. Matter* **4** 10 385
[16] Kunkel H P, Roshko R M and Williams G 1998 *Phys. Rev.* B **37** 5880
[17] Roshko R M and Williams G 1984 *J. Phys. F: Metal Phys.* **14** 703
[18] Williams G 2001 *J. Alloys Compounds* **326** 36
[19] Le Gouillou L C and Zinn-Justin J 1980 *Phys. Rev.* B **21** 3976
[20] Zhao J H *et al* 2000 *J. Phys.: Condens. Matter* **12** L657
[21] Kaul S and Mohan C V 1994 *Phys. Rev.* B **50** 6157
Kaul S 1985 *J. Magn. Magn. Mater.* **53** 5
[22] Berndt A G *et al* 1999 *Phys. Rev.* B **59** 8391
[23] Harris A B 1974 *J. Phys. C: Solid State Phys.* C **7** 1671
[24] Zhou X Z *et al* 1997 *Phys. Rev.* B **56** R12714
[25] Binder K and Young A P 1986 *Rev. Mod. Phys.* **58** 801
Hertz J and Fischer K A 1989 *Spin Glasses* (New York: Cambridge University Press)
[26] Preisach F 1935 *Z. Phys.* **94** 277
[27] Bertotti G 1998 *Hysteresis in Magnetism* (New York: Academic)
Song T *et al* 2001 *J. Phys.: Condens. Matter* **13** 3443
[28] Papavassiliou G *et al* 2000 *Phys. Rev. Lett.* **86** 135
Deac I G, Mitchell J F and Schiffer P 2001 *Phys. Rev.* B **63** 172 408
[29] Urushibara A *et al* 1995 *Phys. Rev.* B **51** 14 103
[30] Emin D and Holstein T 1969 *Ann. Phys., NY* **53** 439
Emin D and Liu N L H 1983 *Phys. Rev.* B **27** 4788
Jaime M *et al* 1997 *Phys. Rev. Lett.* **78** 951
Jaime M and Salamon M B 1999 *Physics of Manganites* ed T A Kaplan and S D Mahanti (New York: Plenum)
Franck J P *et al* 1998 *Phys. Rev.* B **58** 5189
Worledge D C *et al* 1998 *Phys. Rev.* B **57** 15 267
[31] Rakhmanov A L *et al* 2001 *Phys. Rev.* B **63** 174 424
[32] Mayor M *et al* 2001 *Phys. Rev. Lett.* **86** 135
[33] Bhattacharya D 2001 *J. Phys.: Condens. Matter* **13** L431
[34] Raffaelle R *et al* 1991 *Phys. Rev.* B **43** 7991
Jaime M *et al* 1996 *Phys. Rev.* B **54** 11 914
[35] Philips J C 1989 *Physics of High-T_c Superconductors* (San Diego, CA: Academic)
[36] Kagan M Yu, Khomshii D I and Mostovoy M V 1999 *Eur. Phys. J.* B **12** 217
[37] Zhao J H *et al* 2001 *J. Phys.: Condens. Matter* **13** 5785
[38] Zhao G *et al* 2000 *J. Phys.: Condens. Matter* **12** L361
Zhao G *et al* 2000 *Phys. Rev. Lett.* **84** 6086